

Alterations in wall shear stress predict sites of neointimal hyperplasia after stent implantation in rabbit iliac arteries

John F. LaDisa, Jr.,^{1,2,3} Lars E. Olson,² Robert C. Molthen,^{2,6} Douglas A. Hettrick,^{2,3} Phillip F. Pratt,⁵ Michael D. Hardel,³ Judy R. Kersten,^{3,5} David C. Warltier,^{2,3,4,5} and Paul S. Pagel^{2,3}

¹Department of Pediatric Cardiology, Stanford University, Stanford, California; and ²Department of Biomedical Engineering, Marquette University, and ³Department of Anesthesiology, ⁴Division of Cardiovascular Diseases, Department of Medicine, ⁵Department of Pharmacology and Toxicology, and ⁶Department of Pulmonary and Critical Care Medicine, Medical College of Wisconsin, and the Clement J. Zablocki Veterans Affairs Medical Center, Milwaukee, Wisconsin

Submitted 1 November 2004; accepted in final form 10 January 2005

LaDisa, John F., Jr., Lars E. Olson, Robert C. Molthen, Douglas A. Hettrick, Phillip F. Pratt, Michael D. Hardel, Judy R. Kersten, David C. Warltier, and Paul S. Pagel. Alterations in wall shear stress predict sites of neointimal hyperplasia after stent implantation in rabbit iliac arteries. *Am J Physiol Heart Circ Physiol* 288: H2465–H2475, 2005. First published January 14, 2005; doi:10.1152/ajpheart.01107.2004.—Restenosis resulting from neointimal hyperplasia (NH) limits the effectiveness of intravascular stents. Rates of restenosis vary with stent geometry, but whether stents affect spatial and temporal distributions of wall shear stress (WSS) in vivo is unknown. We tested the hypothesis that alterations in spatial WSS after stent implantation predict sites of NH in rabbit iliac arteries. Antegrade iliac artery stent implantation was performed under angiography, and blood flow was measured before casting 14 or 21 days after implantation. Iliac artery blood flow domains were obtained from three-dimensional microfocal X-ray computed tomography imaging and reconstruction of the arterial casts. Indexes of WSS were determined using three-dimensional computational fluid dynamics. Vascular histology was unchanged proximal and distal to the stent. Time-dependent NH was localized within the stented region and was greatest in regions exposed to low WSS and acute elevations in spatial WSS gradients. The lowest values of WSS spatially localized to the stented area of a theoretical artery progressively increased after 14 and 21 days as NH occurred within these regions. This NH abolished spatial disparity in distributions of WSS. The results suggest that stents may introduce spatial alterations in WSS that modulate NH in vivo.

computational fluid dynamics; restenosis; computational modeling; computed tomography; image reconstruction; wall shear stress

RESTENOSIS after stent implantation remains a persistent clinical problem (1, 6, 8, 28, 40, 45). The mechanisms of restenosis are incompletely understood, but direct endothelial and smooth muscle cell damage, reduced compliance, and alterations in the distributions of wall shear stress (WSS) within the stented region have been implicated as potential triggering events that stimulate neointimal hyperplasia (11, 19, 44, 47). Vascular damage to the vessel during implantation may be minimized by using an appropriate stent-to-artery deployment ratio (11, 46). The rigid framework of the stent causes differences in compliance between the stented and native regions of the artery, but this stent rigidity provides structural scaffolding that is associated with reduced restenosis rates compared with angioplasty alone (4, 8). Novel stent designs that reduce compliance mismatch at the proximal and distal edges of the stent have also

been developed (2). Previous studies have suggested that there may be a correlation between stent-induced alterations in WSS and neointimal hyperplasia during pathological processes including primary atherogenesis and restenosis after angioplasty (17, 18, 20, 21, 30). However, few studies have examined detailed time- and space-dependent distributions of WSS or attempted to correlate these alterations in WSS with neointimal hyperplasia after stent implantation in vivo. Moreover, it is well known that restenosis varies with stent geometry (11, 32, 35, 50), but the geometric influence of stent properties on spatial and temporal WSS patterns has not been thoroughly investigated. Thus we tested the hypothesis that local alterations in spatial WSS associated with stent implantation temporally predict sites of neointimal hyperplasia in vivo. We used microfocal X-ray computed tomographic (CT) arterial reconstruction and three-dimensional (3-D) computational fluid dynamics (CFD) modeling to test this hypothesis and correlated these findings with tissue histology in normal rabbit iliac arteries after stent implantation.

METHODS

Use and care of animals. All experimental procedures and protocols used in this investigation were approved by the Animal Care and Use Committee of Marquette University and the Medical College of Wisconsin. Furthermore, all conformed to the American Physiological Society's "Guiding Principles in the Care and Use of Animals" and the National Institutes of Health *Guide for the Care and Use of Laboratory Animals* (7th ed., Washington, DC: Natl. Acad. Press, 1996).

Antegrade iliac artery stent implantation. Antegrade iliac artery stent implantation was performed as previously described (20). Briefly, stent implantation was performed under sterile conditions using a portable fluoroscopic imaging system (OEC, GE Medical Systems; Milwaukee, WI). Anesthesia was induced in male New Zealand White rabbits ($n = 22$) with intravenous xylazine (2.2 mg/kg) and ketamine (22 mg/kg) and maintained with 1–2% isoflurane in oxygen after endotracheal intubation. Rabbits were allowed to breathe spontaneously during the procedure. A 5-Fr introducer sheath was inserted into the left carotid artery through a small incision, and a fluid-filled 5-Fr JR3.5-5 softtip guide catheter preloaded with a guide wire was advanced into the distal descending aorta. The guide wire was advanced into the proximal portion of the right iliac artery, and the guide catheter was carefully removed while the wire remained in place. The stent delivery system was advanced to the distal portion of the iliac artery using the guide wire, and the stent was deployed using

Address for reprint requests and other correspondence: P. S. Pagel, Medical College of Wisconsin, MEB-M4280, 8701 Watertown Plank Rd., Milwaukee, Wisconsin 53226 (E-mail: pspagel@mcw.edu).

The costs of publication of this article were defrayed in part by the payment of page charges. The article must therefore be hereby marked "advertisement" in accordance with 18 U.S.C. Section 1734 solely to indicate this fact.

a pressure of 5 atm to achieve a stent-to-artery size ratio range of 1.1 to 1.2:1 (11). Intravenous heparin (100 U/kg) was administered immediately after stent deployment (43). Successful deployment was verified by angiography, and the stent delivery catheter was removed. The contralateral iliac artery served as the control. The carotid artery was ligated, the incision was closed in layers, and the rabbit was allowed to emerge from anesthesia. Intramuscular buprenorphine (0.05 mg/kg bid) was used for postoperative analgesia. Rabbits received antibiotic prophylaxis (5 mg/kg enrofloxacin) for 4 days after stent implantation and aspirin in their drinking water (20 mg/day) for the duration of the experimental protocol (43).

Experimental groups and stent properties. Sixteen stents were implanted in the iliac arteries of two experimental groups distinguished by the length of stent implantation (14 or 21 days, $n = 8$ rabbits/group). Six additional rabbits underwent carotid artery surgery without stent implantation (control). Prototype stainless steel slotted-tube stents 16 mm in length were delivered using standard over-the-wire or rapid-exchange stent delivery devices mounted on 3.0×16 - or 3.0×20 -mm angioplasty balloons.

Histological analysis. Rabbits designated for histological analysis of stented and unstented arteries underwent iliac artery stent implantation as described above and were killed 14 or 21 days after deployment as discussed previously. The proximal and distal ends of the iliac arteries were identified, and the vessels were excised and fixed in Carnoy's solution for 4 h (44). Samples were then embedded in glycol methyl methacrylate (Technovit 7100, EB Sciences; Agawam, MA) and sectioned at room temperature in 5- μ m intervals using a microtome equipped with a tungsten carbide knife that facilitated direct sectioning through the stent (Delaware Diamond Knives, Ted Pella; Redding, CA). Hematoxylin and eosin staining was used to identify nuclei, cytoplasmic structures, and extracellular components in stented and unstented arterial sections. Light photomicrographs were obtained using a Nikon Optiphot-2 microscope (Tokyo, Japan) equipped with a Diagnostics SPOT charge-coupled device camera (Sterling Heights, MI). The percentage of the vascular lumen in which neointimal hyperplasia had occurred was calculated by subtracting the luminal area at harvest from that bounded by the stent using ImageJ image processing and analysis software (NIH, <http://rsb.info.nih.gov/ij/>). Neointimal hyperplasia was quantified within a 0.5-mm region from both the proximal and distal edges of the stent and in the middle of the stented region.

Hemodynamic data acquisition and iliac artery casting. Rabbits used to classify temporal alterations in WSS after stent implantation were anesthetized as described above 14 or 21 days after stent implantation. The abdomen was opened through a midline incision, and the iliac arteries were carefully dissected free of surrounding connective tissue. A transit-time ultrasonic blood flow transducer

(Transonic Instruments) was used to obtain digital waveforms of blood flow within the descending aorta and iliac arteries proximal to the location of the stent for a minimum of 25 cardiac cycles. The analog signal was gained to a dynamic range of 5 V and fed into a 2-channel, 12-bit analog-to-digital data-acquisition system (232M2A0CT, Integrity Instruments; Pine River, MN). The 4-Hz signal was sampled at 500 Hz in the continuous stream mode using the PCMCIA port on a laptop computer (Compaq Presario 920US 1.6 MHz with 1 GB of RAM). The blood flow time series were lowpass filtered in Matlab using a second-order Butterworth filter with a cutoff frequency of 50 Hz. Representative blood flow waveforms in the descending aorta and proximal iliac arteries during a single cardiac cycle were then constructed using a previously designed Matlab program to spatially align, segment, and ensemble average the collected data (19).

Rabbits were killed using an intravenous overdose of pentobarbital sodium (10 mg/kg), and heparinized saline was administered to prevent thrombus formation. Peripheral aortic and iliac artery branches were ligated. The internal iliac arteries were undisturbed because pilot experiments suggested that ligation of these vessels may introduce anatomic distortion near the bifurcation. Silk ligatures were placed around the proximal end of each femoral artery for subsequent use during the casting procedure, and the distal end of each femoral artery was incised to minimize resistance to the flow of casting media. Baton's No. 17 Corrosion Compound (Polysciences; Warrington, PA) was then injected into the distal aorta and iliac arteries using a perfusion pressure of 100 mmHg, and the femoral arteries were ligated proximally. After being cured, the artery and connective tissues were caustically removed (Polysciences maceration solution), leaving the flow domain cast and stent. The stent was removed, and small branches were removed using a deformable 300-grit sanding pad (33), revealing the flow domain in the distal descending aorta and iliac arteries (Fig. 1).

Microfocal X-ray CT and vascular reconstruction. The iliac artery casts were imaged using a microfocal X-ray CT imaging system. Geometrically accurate reconstruction volumes were generated using the Feldcamp cone-beam reconstruction algorithm (7). Data acquisition, preprocessing, and reconstruction were implemented as previously described (13, 14). A ring artifact reduction (RAR) algorithm was also incorporated into the reconstruction. Briefly, the iliac artery casts were inverted and placed on a rotating stage within the X-ray beam (Fig. 2). A charge-coupled device camera captured the images produced by the image intensifier. Thirty projection images were captured and averaged to generate a single image (512×512 pixels) at each of 360 rotation angles obtained in 1° increments. Spatial errors caused by the magnification process within the image intensifier were removed using previously validated methods (13, 14). The images were then aligned along the center of rotation and processed to

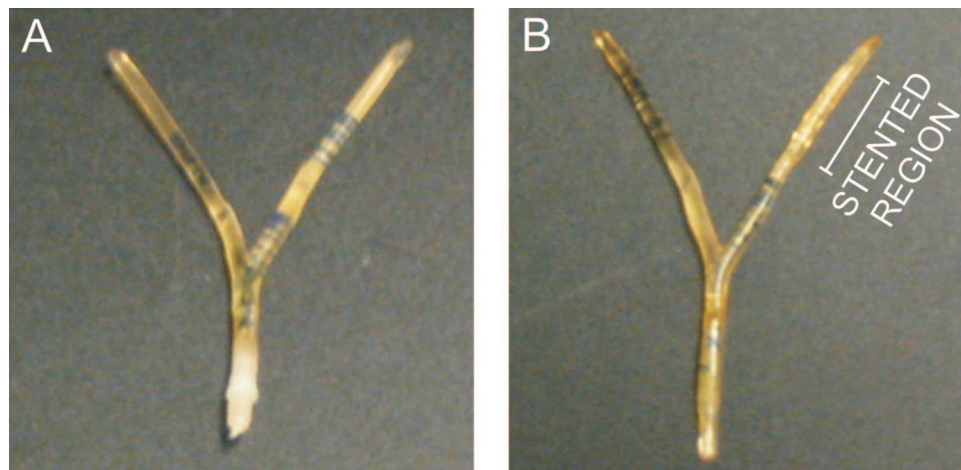


Fig. 1. Representative plastic casts of the distal descending aorta and iliac artery flow domain in rabbits. The cast in A was obtained from a control rabbit in which neither iliac artery was stented. The cast in B was obtained 21 days after unilateral antegrade iliac artery implantation of a 16-mm slotted-tube stent in the right iliac artery.

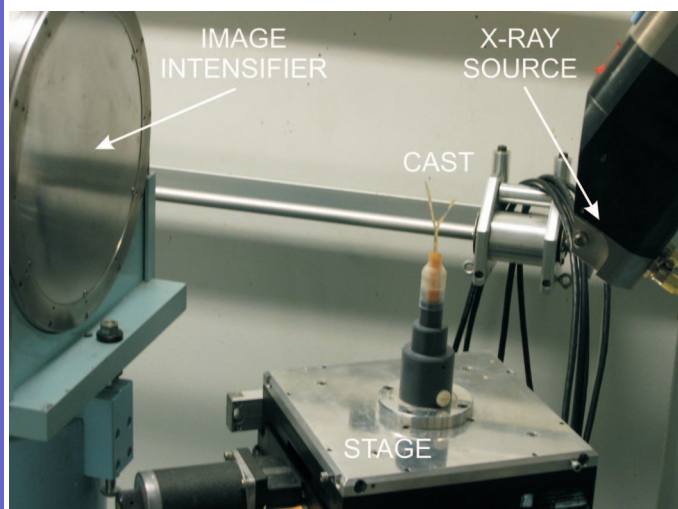


Fig. 2. Microfocal X-ray computed tomography imaging system and cast of a rabbit distal descending aorta and iliac arteries.

remove any spatial and temporal heterogeneity within the X-ray beam. Camera pixels with nonlinear gain or non-zero offset characteristics have the potential to introduce circular streaking artifacts when a reconstruction volume is sectioned perpendicular to the axis of rotation. These artifacts were eliminated using a generalized RAR algorithm (41) before cone-beam reconstruction of the casts. The averaged projection images from each rotation angle were reconstructed to produce isotropic volumes containing 122,763,473 (497^3) voxels (13, 14). High-magnification reconstruction volumes were also generated to increase the geometric magnification within the stented portion of the vessel. The subsequent generation of detailed computational meshes used geometric information from a combination of the low- and high-magnification reconstructions (Fig. 3). Polyethylene tubing of a known diameter was inserted at the base of each artery for use in calibration during the reconstruction. The source-to-artery distances were ~ 15 and 30 cm for the low- and high-magnification scans, respectively, and the distance from the X-ray source to the image intensifier was ~ 91 cm. Reconstructed vascular volumes were rendered using commercially available software (42) (Analyze 5.0, AnalyzeDirect; Lenexa, KS).

CFD mesh generation of reconstructed iliac arteries. Reconstructed volumes were subjected to a series of postprocessing operations in preparation for determining distributions of WSS including iliac artery thresholding, identification of the arterial wall, spatial sorting of points along the luminal surface, and circumferential and axial surface smoothing. Reconstructed volumes were digitally sectioned perpendicular to the axis of rotation to generate 497 unsigned 8-bit integer arrays using Unix script files. The images were then adjusted to use the full dynamic range (0–255 grayscale levels), and an image threshold was implemented using an automated program designed in Matlab. Discontinuities within the binary images were filled using the *infill* function within the image processing toolbox of Matlab. The *bwlabel* and *stats* functions were used to define and record the properties of objects in successive cross-sectional images. The area was obtained for each object in a binary image slice. As a precaution, the algorithm used to determine this area automatically discarded objects $< 50\%$ of the largest object in each image slice. This feature did not influence radius values obtained from reconstruction volumes used in the current investigation, as side branches were processed before being imaged, but was included as a provision for future investigations. The iliac artery bifurcation was defined as the location where the number of objects increased from one to two. The location of the centroids of each object was then calculated and used to delineate between objects in each iliac artery. Objects in successive

cross-sectional slices were assigned to branches based on the minimum distance of the centroids corresponding to objects in the current slice with respect to those in the previous slice. The Sobel method of edge detection was then applied in Matlab to create arrays corresponding to points along the edge of each artery. The coordinates corresponding to each slice of the iliac arteries were spatially aligned for use with automated smoothing and CFD mesh generation programs. Coordinates representing the slices that comprised each vessel were centered about the origin and divided into quadrants. The coordinates in each quadrant were sorted in the *y*-axis followed by the *x*-axis to proceed clockwise. The points in each quadrant were then combined into a common matrix and once again centered about the midline of each iliac artery. Circumferential and axial smoothing was performed according to previously described methods (27). Postprocessing methods were validated by comparing the disparity between distributions of WSS obtained from theoretical vessels containing 4, 8, 12, and 16 surface perturbations before and after surface smoothing. The WSS disparity was plotted as a function of surface perturbation number to create a transfer function that provided important information about the confidence of WSS patterns generated for reconstructed arteries.

Radius values from the reconstructed and processed iliac arteries were imported into a custom-designed automated mesh generation program in Matlab after surface smoothing. Additional length (AL) was added to each artery to ensure that there was a fully developed flow profile at the inlet of the stented region using the equation $AL = 0.06 \cdot Re \cdot d$, where *Re* is the Reynolds number and *d* is the vessel inlet diameter (9). The radius values for the added inlet length were constant and equal to the average radius of the first slice of each iliac artery. A 50:50 flow split was assumed for all computational arteries (29) and was confirmed from *in vivo* blood flow measurements (data not shown). Thus inlet length was added in the flow direction of the descending aorta to mimic the shape of the velocity profile at the inlet

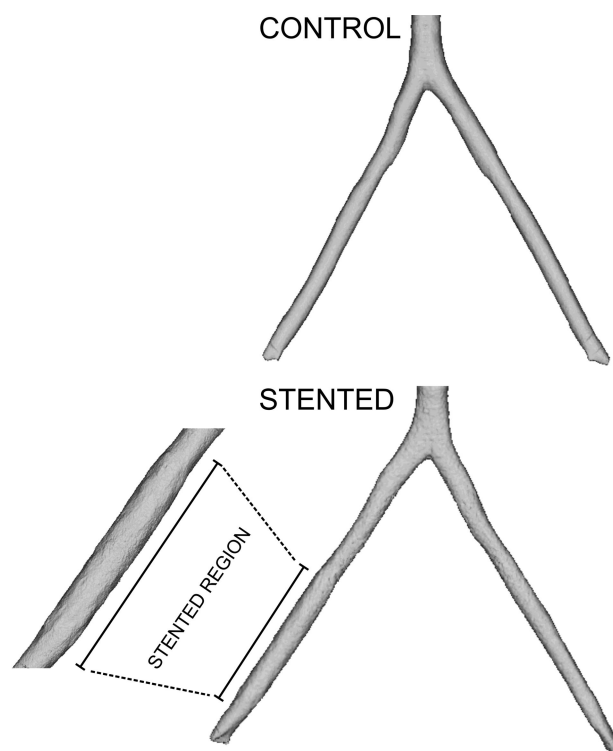


Fig. 3. Representative renderings of the distal descending aorta and iliac arteries from control (*top*) or stented (*bottom*) rabbits after reconstruction using the Feldcamp cone-beam algorithm. Rendering of a high-magnification reconstruction is shown in the *inset* adjacent to the stented iliac artery.

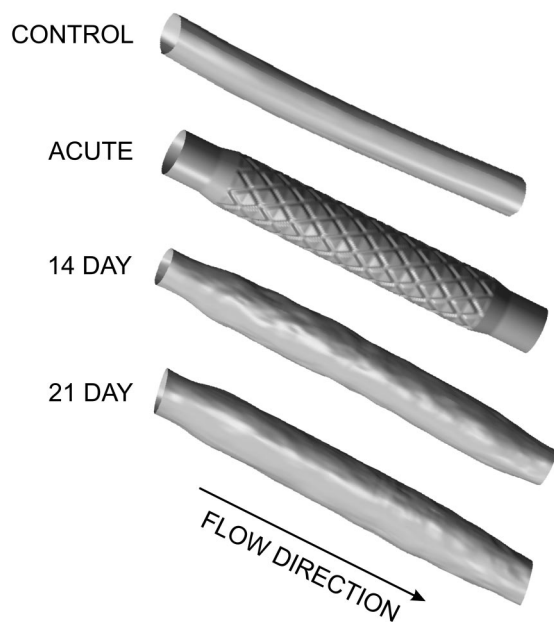


Fig. 4. Representative computational geometries of the reconstructed iliac artery flow domain. The in vivo flow domain in control arteries is depicted next to the theoretical flow domain after acute stent implantation and that obtained from arteries 14 and 21 days after stent implantation.

of the iliac arteries, without modeling the descending aorta itself. This assumption provided more computational nodes and improved spatial resolution within the distal stented region of the artery. AL was also added to the outlet of the vessels to account for exit effects. The radius values for the AL at the outlet were equal to those of the last arterial slice. Computational meshes for stented iliac arteries were generated using the low- and high-magnification reconstructions. This process facilitated the creation of very fine computational meshes that were required to capture subtle variations on the surface of the vascular casts. Thus the resolution proximal and distal to the stented region was modestly reduced, and arbitrary interface boundary conditions were implemented using the commercially available software package CFD-ACE+ (CFDRC; Huntsville, AL) to increase the circumferential and axial resolution within the stented region to ~ 32 and $50 \mu\text{m}$, respectively. Representative flow domains in control and stented iliac arteries obtained from microfocal X-ray CT imaging, reconstruction, and postprocessing are shown in Fig. 4. The theoretical iliac artery after acute stent implantation shown in Fig. 4 was created as discussed previously using the strut thickness and width, length, and diameter of the stent implanted in vivo (21).

Determination of indexes of WSS. Computational simulations were performed using CFD-ACE+. This software uses a finite-volume approach to solve the continuity and Navier-Stokes equations at the center of each hexahedral control volume. Blood was modeled as a Newtonian incompressible fluid with a constant viscosity of 3.7 cP and density of 1.060 g/cm^3 (18, 36). The mean velocity obtained from the representative in vivo iliac artery waveform shown in Fig. 5 (24 mm/s) was imposed as plug flow at the inlet of each vessel. This inlet boundary condition corresponds to a Re of ~ 17 and is consistent with blood flow in the rabbit iliac arteries under steady-state resting conditions. Simulations were allowed to converge for a minimum of 400 iterations or a 10^{-4} reduction in the solution residuals. Distributions of WSS in control and stented iliac arteries were then calculated by the CFD-ACE software package using the second invariant of the

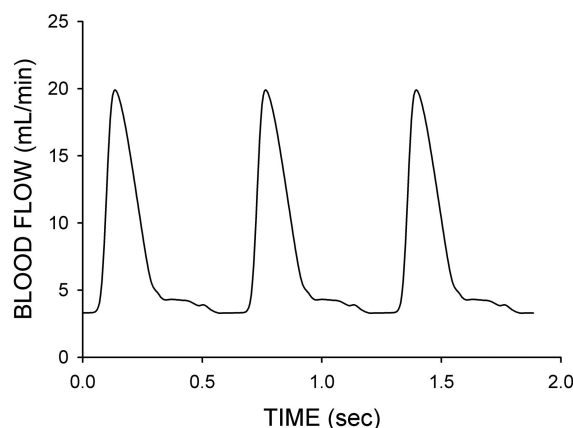


Fig. 5. Representative blood flow time series from the proximal iliac artery of an anesthetized rabbit.

rate of deformation tensor as discussed previously (18) and shown below

$$\gamma = \{2[(\partial u/\partial x)^2 + (\partial v/\partial y)^2 + (\partial w/\partial z)^2] + (\partial u/\partial y + \partial v/\partial x)^2 + (\partial u/\partial z + \partial w/\partial x)^2 + (\partial v/\partial z + \partial w/\partial y)^2\}^{1/2}$$

where u , v , and w are the x , y , and z components of velocity vector \mathbf{u} , respectively. WSS results within the stented region of the iliac artery were normalized to the average WSS value in the contralateral unstented iliac artery to account for potential differences in iliac artery length and diameter between rabbits. Spatial WSS gradients (WSSG) were also calculated during postprocessing as described previously (21) using the equation $[(\partial \tau_{w,z}/\partial z)^2 + (\partial \tau_{w,\theta}/\partial \theta)^2]^{1/2}$, where $\tau_{w,z}$ and $\tau_{w,\theta}$ are WSS in the axial and circumferential directions, respectively.

The temporal adaptation of spatial distributions of WSS within the stented region 14 and 21 days after implantation was investigated using localized averages of five adjacent control volumes at seven axial sites along the medial and lateral luminal surface as described previously and illustrated in Fig. 6 (29). These values were normalized by the respective groups of control volumes in the contralateral control artery. This method illustrates changes in the spatial and temporal behavior of WSS but alleviates errors introduced by direct spatial comparisons between simulation results in contralateral arteries.

The influence of physical forces 14 and 21 days after stent implantation was obtained by plotting the change in radius as a function of WSS or WSSG within the stented region of the vessel. A normalization factor was introduced to account for the elliptical shape of sequential transaxial slices, and the change in radius (Δr_{norm}) was

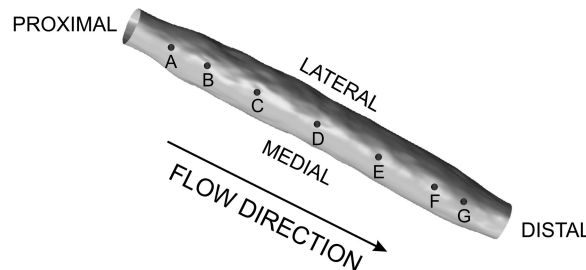


Fig. 6. Schematic drawing illustrating the locations (A–G) for determination of spatial distributions of wall shear stress (WSS) within the stented region. The mean WSS at 7 axial locations along the medial and lateral iliac artery luminal surfaces was calculated using localized averages of 5 adjacent control volumes on the vascular wall and normalized to the respective groups of control volumes in the contralateral unstented artery.

calculated within the stented portion of the iliac arteries using the equation $\Delta r_{\text{norm}} = (r_i - r_o/r_o) \cdot r_{\text{min}}$, where r_o is a representative radius from the proximal unstented portion of the iliac artery, r_i denotes the axial slice of interest, and r_{min} is the minimum radius within the slice. The slope of normalized WSS or WSSG versus the change in vessel radius was then determined for each stented iliac artery by linear regression analysis.

Statistical analysis. Statistical analysis within and between groups was conducted using multiple ANOVA for repeated measures followed by application of the Student-Newman-Keuls test. Changes within and between groups were considered statistically significant when $P < 0.05$. All data are expressed as means \pm SE.

RESULTS

Histology. Stent implantation was not associated with aortic injury and had no detectable influence on contralateral unstented iliac or distal femoral arteries as demonstrated by intact endothelial, internal elastic lamina, and medial layers in histological cross sections (20). In contrast, neointimal hyperplasia occurred within the stented portion of the artery and was greater at the proximal end compared with the middle and distal ends of each stent independent of the length of implantation (Fig. 7). The amount of neointimal hyperplasia was less pronounced in the middle of the stented segments. Modest

increases in the luminal percentage of neointimal hyperplasia occurred in stents implanted for 21 compared with 14 days with the exception of the proximal region of the stent (Fig. 7).

Theoretical spatial distributions of WSS immediately after stent implantation and corresponding temporal changes in vessel histology are summarized in Fig. 8. Neointimal hyperplasia was particularly pronounced in the proximal and distal stent-to-artery transition regions. There was a strong correlation between areas of low WSS predicted by the theoretical artery immediately after stent implantation and the localization of neointimal hyperplasia in the histological sections. Specifically, the theoretical computational vessel illustrating normalized distributions of WSS in Fig. 9 demonstrated that regions adjacent to stent struts are exposed to low WSS immediately after implantation. Two representative histological sections from the middle section of the stent shown in Fig. 9 indicated that these areas of low WSS contained greater neointimal hyperplasia than areas that are subjected to higher WSS.

Mesh independence. Stent placement did not alter proximal iliac artery blood flow, and no differences in iliac artery blood flow were observed between experimental groups (data not shown). Thus the mean blood flow velocity value corresponding to a representative iliac artery blood flow waveform (24

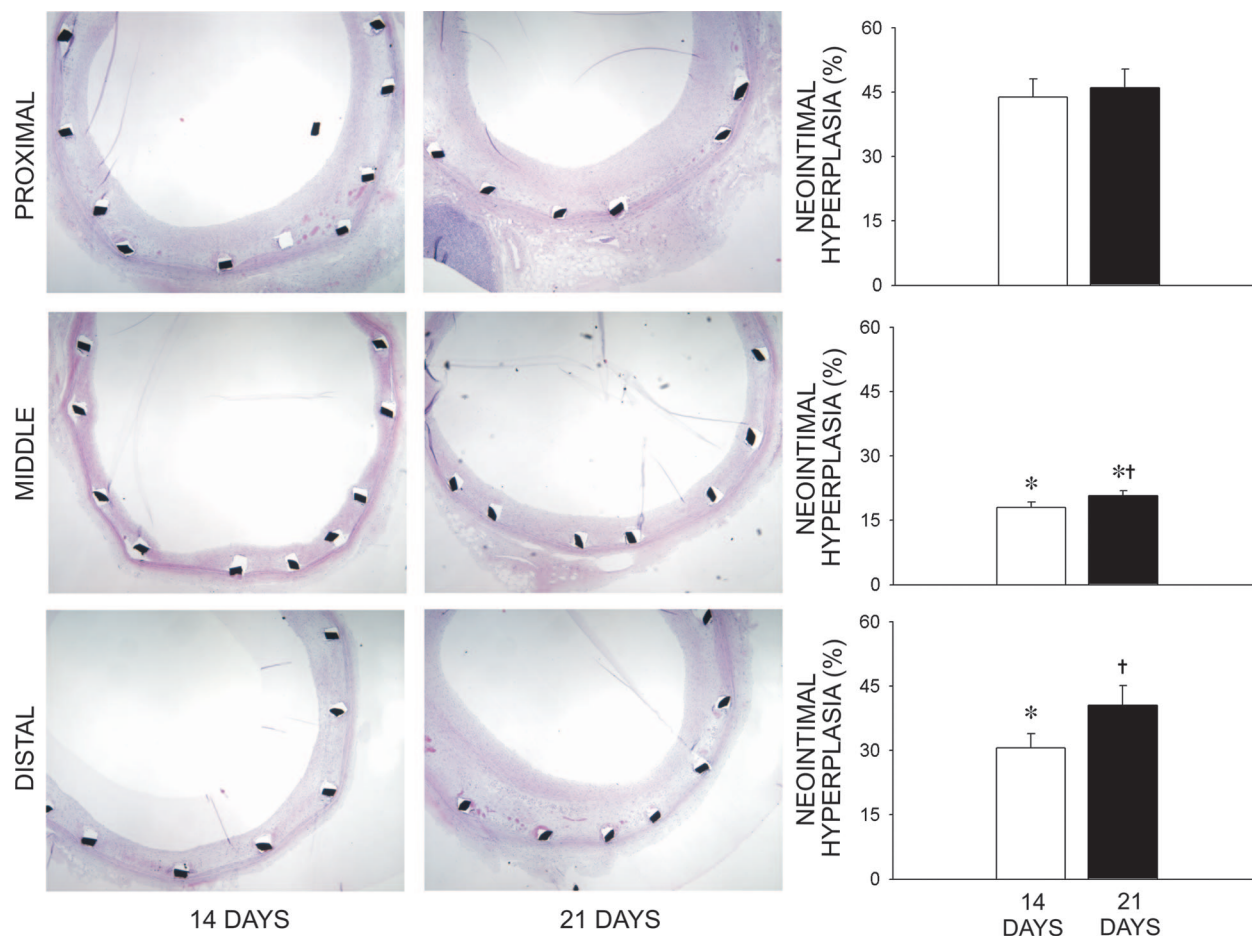


Fig. 7. Representative photomicrographs of 5- μ m vascular cross sections stained with hematoxylin and eosin. The sections illustrate neointimal hyperplasia within 0.5-mm regions in the proximal (top row), middle (middle row), or distal (bottom row) portions of stents implanted into rabbit iliac arteries for 14 or 21 days. Histograms depict the percentage of the luminal area experiencing neointimal hyperplasia. *Significantly ($P < 0.05$) different from proximal in the respective group; †significantly ($P < 0.05$) different from the percentage of neointimal hyperplasia within the stented region 14 days after implantation.

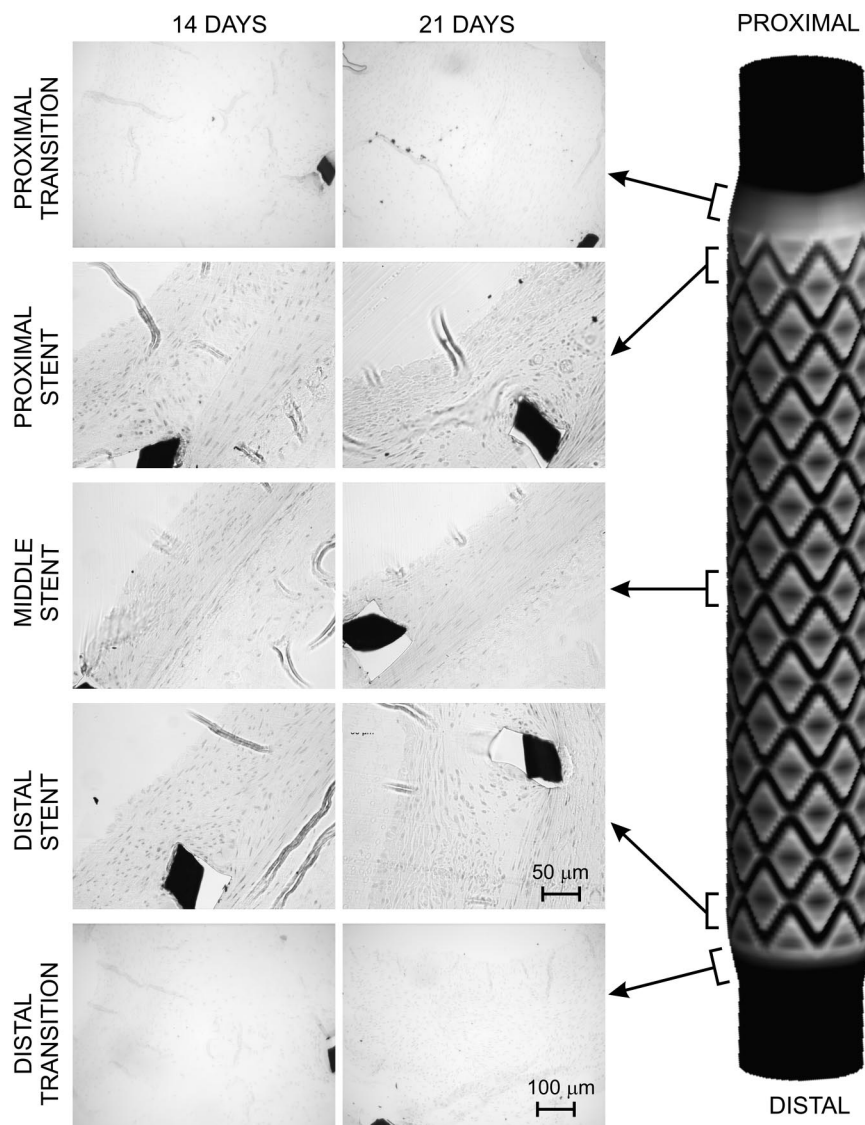


Fig. 8. Histological cross sections stained with hematoxylin and eosin at various spatial locations proximal and distal to ($\times 10$) and within the stented portion of an iliac artery ($\times 20$). Iliac artery cross sections are arranged with the vascular lumen orientated toward the top left corner of each image.

mm/s; Fig. 5) was used as the input boundary condition to the steady-state CFD models. Guidelines establishing adequate computational mesh densities required to obtain WSS determinations have been previously validated (38) and were followed in the current investigation. Mesh independence was investigated by sequentially increasing the number of circumferential and axial nodes until there were no appreciable differences in the distributions of WSS between successive converging solutions. Approximately 350,000 nodes were used for control iliac arteries. Extremely fine computational meshes were required to capture alterations on the surface of the vascular casts generated from stented iliac arteries. Therefore, the mesh density upstream and proximal to the local stented region was slightly compromised to increase the circumferential and axial resolution to ~ 32 and $50 \mu\text{m}$, respectively, within the stented region. As a result, computational meshes representing stented iliac arteries contained an average of 588,214 nodes, of which $>90\%$ were dedicated to the region of the stent. The minimum and maximum number of nodes used to represent stented iliac arteries was

492,913 and 709,192, respectively. Figure 10 suggests that it is highly unlikely that conclusions about alterations of WSS in iliac arteries after stent implantation would have been substantially affected by further increases in computational mesh density.

Indexes of WSS. Normalized distributions of WSS in iliac arteries before and 14 or 21 days after stent deployment are illustrated beside the theoretical distribution of WSS immediately after implantation in Fig. 11. The normalized distribution of WSS was approximately one throughout control iliac arteries. Conversely, stent implantation caused a reduction in WSS within this region as a result of the increased luminal diameter necessary for vascular scaffolding. Low WSS in localized regions of the theoretical stented artery progressively increased after 14 and 21 days. Moreover, spatial disparity in the distributions of WSS caused by the intricacies of the stent after acute implantation was attenuated after 14 and 21 days.

Localized groups of control volumes were used to quantify these alterations in WSS at seven axial locations within the

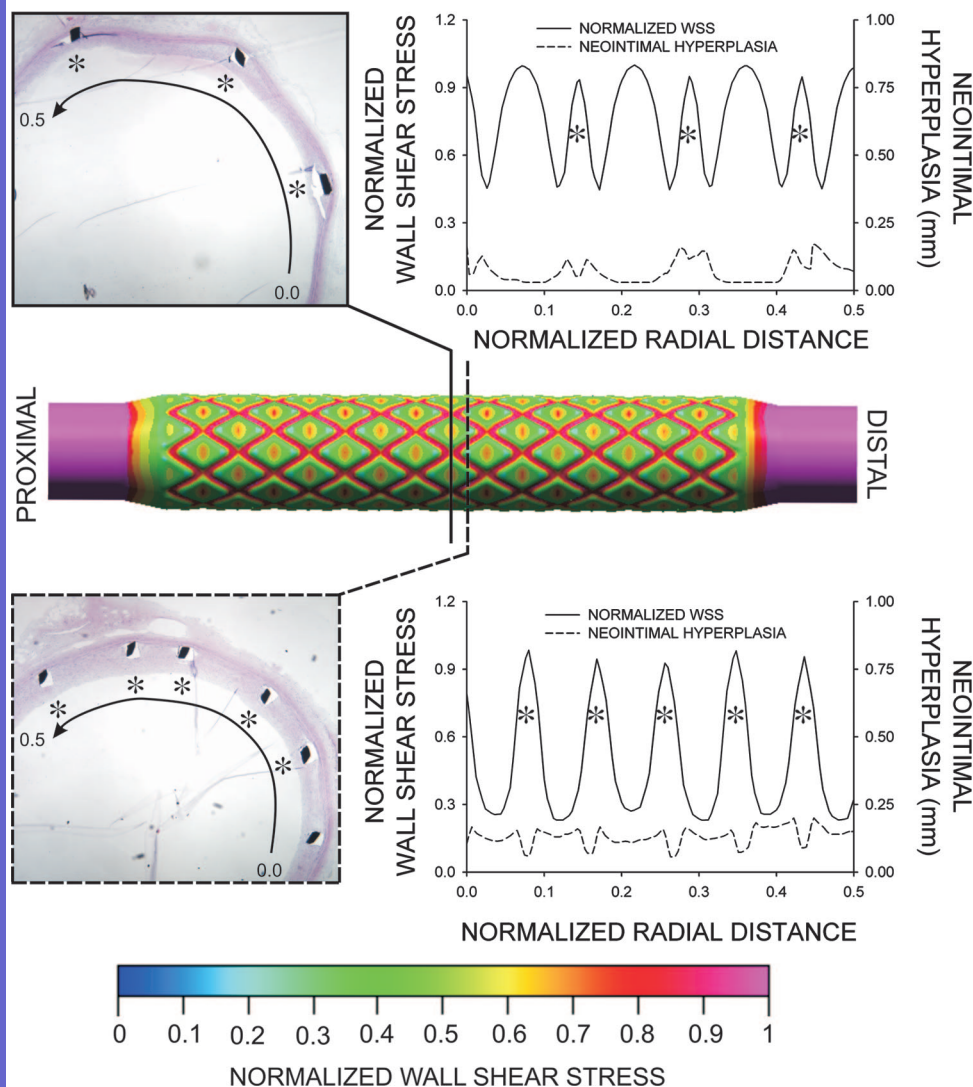


Fig. 9. Predicted areas of WSS immediately after stent deployment and the localization of neointimal hyperplasia in histological sections 14 days after implantation. The computational model (middle) predicts that regions adjacent to stent struts are exposed to low WSS immediately after implantation. Histological sections from the middle section of the stent (top and bottom) verify that these predicted areas of low WSS contain a greater amount of neointimal hyperplasia than areas subjected to higher WSS. Plots of normalized WSS and neointimal hyperplasia as a function of normalized radial distance demonstrated a correlation between localized stent-induced alterations in the artery cross section and distributions of WSS after implantation and the subsequent development of neointimal hyperplasia (see text). *Locations of stent struts.

stented region (Fig. 12). There were no differences in WSS at any of the axial locations for control iliac arteries. No differences were observed between WSS values at the proximal and distal stent-to-artery transitions on the medial or lateral sur-

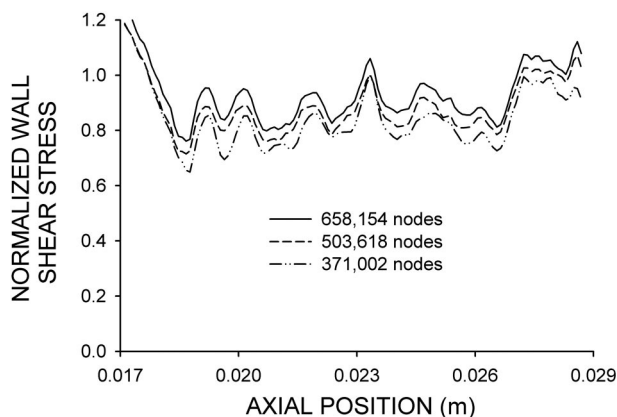


Fig. 10. Representative axial distributions of normalized WSS in the stented portion of an iliac artery constructed from successively denser computational meshes.

faces 14 or 21 days after stent implantation (locations A and G). Conversely, distributions of WSS within the stent were attenuated after 14 days along the medial and lateral luminal surfaces. Reductions in WSS persisted 21 days after implantation along the medial luminal surface distal to the midpoint of stented compared with control iliac arteries (Fig. 12, top). Similarly, WSS was reduced along the lateral luminal surface of the stented region compared with control iliac arteries 21 days after implantation (Fig. 12, bottom). Low WSS in localized regions of the theoretical stented artery increased in a time-dependent manner in four locations along the medial and two locations along the lateral luminal surfaces (Fig. 12, top and bottom, respectively). Spatial WSSG resulting for acute stent implantation were attenuated and similar 14 and 21 days after stent implantation, as demonstrated in Fig. 13.

Distributions of WSS were inversely related to the change in vessel radius for all rabbits, and there was a decrease in the severity of the slope of this relationship from 14 to 21 days (14 days: $-1,462 \pm 161$ vs. 21 days: $-1,125 \pm 171$, $P < 0.05$). In contrast, WSSG was not related to the change in vessel radius (14 days: $-54,524 \pm 12,039$ vs. 21 days: $-33,179 \pm 7,660$, $P = 0.19$).

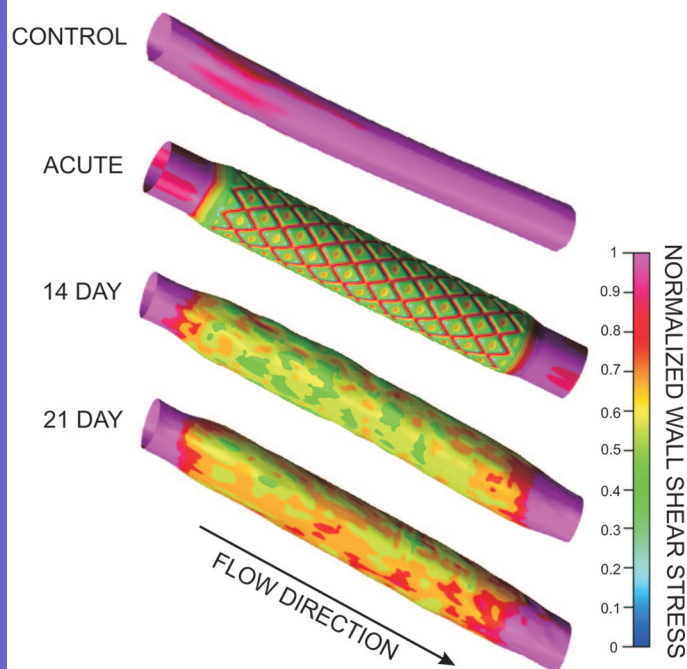


Fig. 11. Representative distributions of normalized WSS in control and stented iliac arteries. The *in vivo* distribution of WSS in a control artery is depicted next to that in an acutely stented, theoretical vessel and that obtained from stented arteries 14 and 21 days after stent implantation.

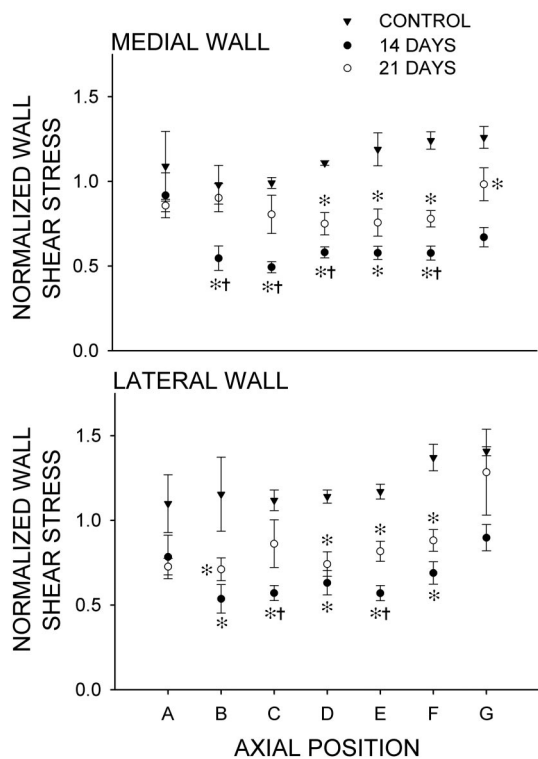


Fig. 12. Normalized WSS along the medial (*top*) and lateral (*bottom*) luminal surfaces within the stented portion of iliac arteries at the 7 axial locations depicted in Fig 6. Values are means \pm SE. *Significantly ($P < 0.05$) different from WSS in control arteries; †significantly ($P < 0.05$) different from WSS within the stented region 21 days after implantation.

DISCUSSION

The influence of stent geometry on local distributions of WSS has only been recently explored. WSS mediated the rate of endothelial and smooth muscle cell migration and proliferation in a model of vascular injury in which a microcylinder was implanted orthogonal to blood flow in the rat vena cava *in vivo* (23, 26). The analytic solution for the distribution of WSS across the cylinder was correlated with the spatial location and temporal dependence of cellular growth (23, 26). Neointimal hyperplasia, the spatial clustering of cells, and expression of several molecular mediators of proliferation were observed at stagnation points and in regions of low WSS along the cylinder. In contrast, these findings were absent in areas of elevated shear stress along the cylinder and after pharmacological inhibition of cellular proliferation (24, 25). These findings suggested that neointimal hyperplasia occurs in regions of low WSS *in vivo*. The results of this previous study also indirectly suggested that stent geometries designed to minimize regions of low WSS after implantation may limit subsequent cellular proliferation.

The current investigation confirms and extends the findings of Liu et al. (23–26) and validates our previous computational results (18, 20, 21). The current results demonstrate that time-dependent neointimal hyperplasia occurred in regions displaying the lowest initial values of WSS predicted by 3-D CFD modeling of a theoretical artery. Progressive neointimal hyperplasia corresponding to spatial locations of initially reduced WSS also caused an increase in the overall WSS within the stented region and reestablished a circular luminal cross section. The initial distribution of WSS after acute implantation resulting from the arrangement of adjacent struts and vascular scaffolding dictated which areas within the artery experienced the greatest growth during this process. Struts in closest radial proximity limited vascular protrusion into the

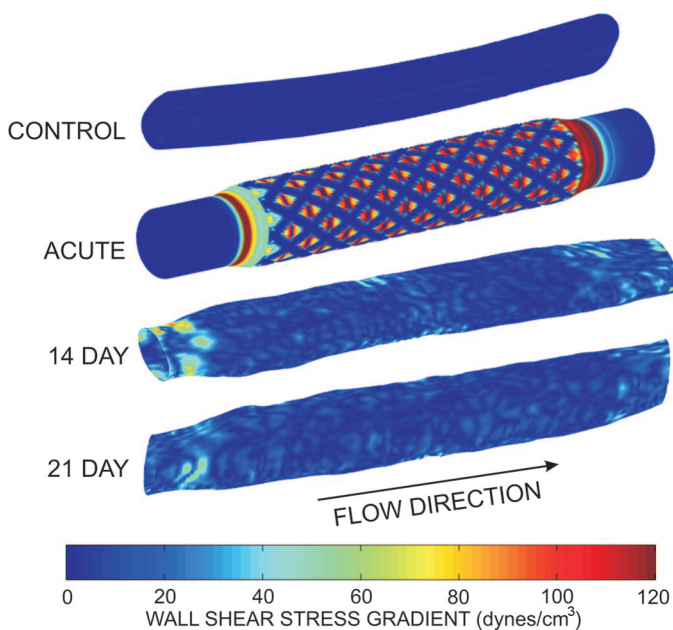


Fig. 13. Representative spatial WSS gradients in iliac arteries 14 and 21 days after stents implantation. The *in vivo* distribution of WSS gradients in a control artery is depicted next to that in an acutely stented, theoretical vessel and that obtained from stented arteries 14 and 21 days after stent implantation.



flow domain, increased the cross-sectional area, and reduced blood velocity resulting in localized areas of low WSS with elevated neointimal hyperplasia. Conversely, struts further from one another promoted intrastrut areas of high WSS that limited neointimal hyperplasia.

The current results indicate that there is an inverse relationship between the temporal change in arterial radius and WSS. The temporal dependence of this relationship suggests that cellular growth after stenting is dependent on distributions of WSS produced by the implanted stent and is greatest immediately after implantation. This temporal histological response to the presence of the stent may resemble the decaying exponential description of intimal thickness in the human carotid artery (16). The current data further suggest that cellular proliferation occurs in response to imposed low WSS, thereby restoring distributions of WSS to an "average" value observed under quiescent physiological conditions within the artery. The lack of differences in WSSG between 14 and 21 days supports this contention and also indirectly supports the hypothesis that large WSSG play a major role in stimulating neointimal hyperplasia immediately after implantation.

Our laboratory has previously demonstrated that low WSS and elevated spatial WSSG are most pronounced at the proximal entrance of a theoretical stented artery (21). The current results support these previous observations and indicate that elevated spatial WSSG was most pronounced at the inlet and outlet of the stented artery where neointimal hyperplasia was greatest *in vivo*. We have previously shown that a steady-state inlet boundary condition corresponding to mean blood flow velocity reasonably approximated the average distributions of WSS in a stented artery (22). This theoretical investigation also suggested that the intrastrut area of low WSS was most pronounced at the inlet of the vessel throughout the cardiac cycle regardless of the number of stent struts or vessel geometry after deployment. Thus these previous results support the current observation that the percentage of neointimal hyperplasia in the proximal portion of the stent did not progressively increase 14 compared with 21 days after implantation.

Neointimal hyperplasia is most prevalent in regions where the native blood flow environment is disturbed as these regions are susceptible to altered mass transport of oxygen, low-density lipoproteins, and cytokines traveling in the blood (39). As demonstrated in the current investigation, stent implantation also causes changes in vascular geometry and influences WSS, but the ability of these changes to differentially influence signal transduction pathways associated with cellular proliferation has not been comprehensively studied. Future studies will elucidate the molecular mediators of neointimal hyperplasia and be used to explain how stent-induced alterations in indexes of WSS are associated with this process.

The current results should be interpreted within the constraints of several potential limitations. The current investigation used a common stent geometry that closely resembled the classic slotted-tube design of the Palmaz-Schatz stent. Previous CFD studies using this geometry demonstrated that flow alterations occurred adjacent to stent struts and were caused by convective acceleration of the fluid as it contacted or passed over the struts (18). These struts were primarily aligned in the axial direction and, therefore, caused modest deflections in the pattern of blood flow by gently redirecting the fluid. This model contrasts with more complex flow deformations that

most likely occur with more intricate stent designs containing several interconnected axially and circumferentially aligned struts. The current findings suggest that the later more elaborate stent designs may cause greater flow disruptions that may be responsible for more pronounced neointimal hyperplasia.

The circumferential and axial resolution used for CFD analysis in rabbit iliac arteries was ~ 32 and $50 \mu\text{m}$, respectively. Increasing the number of images averaged to acquire each projection from 30 to 100 had no appreciable difference on reconstruction quality. Increasing the number of detector pixels to 1024×1024 may have increased circumferential and axial resolution, but such an increase would have resulted in unmanageable amounts of data from a computational perspective. Moreover, the current detector setting of 512×512 pixels was capable of producing computational meshes with more nodes (>1 million) than could be modeled in the CFD environment. The current CFD results from rabbit iliac arteries were obtained using a representative steady-state inlet velocity value obtained from rabbits anesthetized with isoflurane and may differ from that obtained in an awake animal or time-dependent simulations. Unfortunately, the use of transient simulations with arbitrary interface boundary conditions is not currently possible, and eliminating this methodological detail would have introduced severe undersampling of the computational mesh in the stented region of the vessel.

A modest amount of surface variability was introduced during reconstruction of control and stented arteries. Consequently, axial and circumferential smoothing algorithms were implemented before CFD analysis was conducted. To fully characterize the behavior of these postprocessing operations, a transfer function was created by expressing the disparity between distributions of WSS obtained in theoretical vessels containing 4, 8, 12, or 16 surface perturbations before and after smoothing as a function of the perturbation number. The transfer function containing reconstructed 16-mm stents implanted into rabbit iliac arteries for up to 21 days after implantation and resolved at circumferential and axial resolutions of 32 and $50 \mu\text{m}$, respectively, indicated that the present postprocessing techniques are sufficient to resolve distributions of WSS with at least 80% accuracy in stented vascular segments containing 16 surface perturbations over a 16-mm axial length. Distributions of WSS were resolved with 96% accuracy in the current investigation as the slotted-tube stents implanted here contained eight repeating strut units. Thus it appears unlikely that the observed differences between experimental groups were related to a lack of precision in postprocessing operations.

Restenosis after stent implantation in diseased human arteries may differ substantially from neointimal hyperplasia occurring in healthy rabbit arteries. Studies in animal models have shown that neointimal hyperplasia is composed primarily of migrating and proliferating smooth muscle cells with some extracellular matrix (1). Conversely, restenotic lesions in humans are composed principally of extracellular matrix and collagen. The development of neointimal hyperplasia after stent implantation also occurs more rapidly in animals. Reendothelialization of a stented artery in an experimental animal occurs between 21 and 56 days after deployment, but this process may not begin for several months in humans (37, 48). Thus the mechanisms governing WSS-mediated neointimal hyperplasia in the current rabbit model may differ from those occurring clinically. The greatest inflammatory response to



stent implantation is located in regions where the stent lies in apposition to the intima (5, 6), suggesting that the present histological results from normal rabbit iliac arteries also differ from human lesions, which are typically eccentric in shape and place the stent in only partial contact with the calcified atherosclerotic plaque. Despite the differences between animal models of atherosclerosis and the clinical disease process, animal models appear to provide a useful description of the vascular response in humans, albeit in an accelerated time scale (48). Recent studies have demonstrated that drug-eluting stents that limit neointimal hyperplasia in rabbits also reduce restenosis in clinical trials (10, 31). Moreover, many of the current criteria necessary for a stent delivery device to gain Food and Drug Administration approval are based on findings from animal models of vascular injury. Thus the rabbit iliac artery model used in the current investigation is considered to be appropriate for examining vascular responses to stent deployment (1, 34, 37).

Admittedly, WSS is not the only factor involved in the development of neointimal hyperplasia after stent implantation. Vascular inflammation, compliance mismatch, and complex molecular events also result in neointimal growth (1–3, 12, 15, 49). However, in the current investigation where stent implantation was the trigger, resulting distributions of WSS differentially influenced local activation of cells involved in this process.

Minimizing flow disturbances through the stented portion of a vessel is only one of several desirable stent characteristics. Those also of importance include a highly flexible and low-profile stent delivery catheter, increased radiopacity under angiography, limited foreshortening upon deployment, and minimal tissue prolapse into the stented region. Although there is no ideal stent, consideration of stent-induced alterations in local WSS after deployment during the design of these intravascular scaffolds can only help to alleviate the potential for neointimal hyperplasia and subsequent restenosis.

In conclusion, the current results indicate that spatial distributions of WSS produced by stent implantation predict locations of neointimal hyperplasia. The results further indicate that temporal variations in WSS occur as a result of this tissue growth and that these spatial alterations in WSS modulate neointimal hyperplasia and progressively abolish WSS disparity in vivo. Further investigations examining the complex interaction between stent-induced vascular deformation, indexes of WSS, and neointimal hyperplasia may lead to novel stent geometries with flow characteristics that intrinsically inhibit neointimal hyperplasia.

ACKNOWLEDGMENTS

The authors thank Heidi T. Meier (Center for Animal Research Imaging, Medical College of Wisconsin), Steven T. Haworth (Department of Pulmonary and Critical Care Medicine, Medical College of Wisconsin), Kristina M. Ropella and Said H. Audi (Department of Biomedical Engineering, Marquette University), and David Powers and Max Imas (Olin Engineering Center, Marquette University) for technical support and Mary Lorence-Hanke (Department of Anesthesiology, Medical College of Wisconsin) for assistance in the preparation of this manuscript.

GRANTS

This study was supported in part by National Institutes of Health Grants HL-03690 (to J. R. Kersten), HL-63705 (to J. R. Kersten), HL-54820 (to D. C. Warltier), and GM-08377 (to D. C. Warltier) and a Sigma Xi grant-in-aid of research award (to J. F. LaDisa).

REFERENCES

- Bennett MR and O'Sullivan M. Mechanisms of angioplasty and stent restenosis: implications for design of rational therapy. *Pharmacol Ther* 91: 149–166, 2001.
- Berry JL, Manocha E, Mekkaoui C, Rolland PH, Moore JE Jr, and Rachev A. Hemodynamics and wall mechanics of a compliance matching stent: in vitro and in vivo analysis. *J Vasc Interv Radiol* 13: 97–105, 2002.
- Danenberg HD, Welt FG, Walker M, Seifert P, Toegel GS, and Edelman ER. Systemic inflammation induced by lipopolysaccharide increases neointimal formation after balloon and stent injury in rabbits. *Circulation* 105: 2917–2922, 2002.
- Erbel R, Haude M, Hopp HW, Franzen D, Rupprecht HJ, Heublein B, Fischer K, de Jaegere P, Serruys P, Rutsch W, and Probst P. Coronary-artery stenting compared with balloon angioplasty for restenosis after initial balloon angioplasty. Restenosis Stent Study Group. *N Engl J Med* 339: 1672–1678, 1998.
- Farb A, Sangiorgi G, Carter AJ, Walley VM, Edwards WD, Schwartz RS, and Virmani R. Pathology of acute and chronic coronary stenting in humans. *Circulation* 99: 44–52, 1999.
- Farb A, Weber DK, Kolodgie FD, Burke AP, and Virmani R. Morphological predictors of restenosis after coronary stenting in humans. *Circulation* 105: 2974–2980, 2002.
- Feldkamp LA, Davis LC, and Kress JW. Practical cone-beam algorithm. *J Opt Soc Am A* 1: 612–619, 1984.
- Fischman DL, Leon MB, Baim DS, Schatz RA, Savage MP, Penn I, Detre K, Veltri L, Ricci D, and Nobuyoshi M. A randomized comparison of coronary-stent placement and balloon angioplasty in the treatment of coronary artery disease. Stent Restenosis Study Investigators. *N Engl J Med* 331: 496–501, 1994.
- Fox RW and McDonald AT. *Introduction to Fluid Mechanics*. New York: Wiley, 1992.
- Gallo R, Padurean A, Jayaraman T, Marx S, Roque M, Adelman S, Chesebro J, Fallon J, Fuster V, Marks A, and Badimon JJ. Inhibition of intimal thickening after balloon angioplasty in porcine coronary arteries by targeting regulators of the cell cycle. *Circulation* 99: 2164–2170, 1999.
- Garasic JM, Edelman ER, Squire JC, Seifert P, Williams MS, and Rogers C. Stent and artery geometry determine intimal thickening independent of arterial injury. *Circulation* 101: 812–818, 2000.
- Grewe PH, Deneke T, Machraoui A, Barmeyer J, and Muller KM. Acute and chronic tissue response to coronary stent implantation: pathologic findings in human specimen. *J Am Coll Cardiol* 35: 157–163, 2000.
- Karau KL, Johnson RH, Molthen RC, Dhyani AH, Haworth S, Hanger C, Roerig D, and Dawson CA. Microfocal X-ray CT imaging and pulmonary arterial distensibility in excised rat lungs. *Am J Physiol Heart Circ Physiol* 281: H1447–H1457, 2001.
- Karau KL, Molthen RC, Dhyani A, Haworth ST, Hanger CC, Roerig DL, Johnson RH, and Dawson CA. Pulmonary arterial morphometry from microfocal X-ray computed tomography. *Am J Physiol Heart Circ Physiol* 281: H2747–H2756, 2001.
- Kornowski R, Hong MK, Tio FO, Bramwell O, Wu H, and Leon MB. In-stent restenosis: contributions of inflammatory responses and arterial injury to neointimal hyperplasia. *J Am Coll Cardiol* 31: 224–230, 1998.
- Ku DN. Blood flow in arteries. *Ann Rev Fluid Mech* 29: 399–434, 1997.
- Ku DN, Giddens DP, Zarins CK, and Glagov S. Pulsatile flow and atherosclerosis in the human carotid bifurcation. Positive correlation between plaque location and low oscillating shear stress. *Arteriosclerosis* 5: 293–302, 1985.
- LaDisa JF Jr, Guler I, Olson LE, Hettrick DA, Kersten JR, Warltier DC, and Pagel PS. Three-dimensional computational fluid dynamics modeling of alterations in coronary wall shear stress produced by stent implantation. *Ann Biomed Eng* 31: 972–980, 2003.
- LaDisa JF Jr, Hettrick DA, Olson LE, Guler I, Gross ER, Kress TT, Kersten JR, Warltier DC, and Pagel PS. Coronary stent implantation alters coronary artery hemodynamics and wall shear stress during maximal vasodilation. *J Appl Physiol* 93: 1939–1946, 2002.
- LaDisa JF Jr, Meier HT, Olson LE, Kersten JR, Warltier DC, and Pagel PS. Antegrade iliac artery stent implantation for the temporal and spatial examination of stent-induced neointimal hyperplasia and alterations in regional fluid dynamics. *J Pharmacol Toxicol Methods*. Epub ahead of print September 11, 2004.
- LaDisa JF Jr, Olson LE, Guler I, Hettrick DA, Audi SH, Kersten JR, Warltier DC, and Pagel PS. Stent design properties and deployment ratio influence indexes of wall shear stress: a three-dimensional computational

- fluid dynamics investigation within a normal artery. *J Appl Physiol* 97: 424–430, 2004.
22. LaDisa JF Jr, Olson LE, Guler I, Hettrick DA, Kersten JR, Warltier DC, and Pagel PS. Circumferential vascular deformation after stent implantation alters wall shear stress evaluated using time-dependent 3D computational fluid dynamics models. *J Appl Physiol* 98: 947–957, 2005.
 23. Liu SQ and Goldman J. Role of blood shear stress in the regulation of vascular smooth muscle cell migration. *IEEE Trans Biomed Eng* 48: 474–483, 2001.
 24. Liu SQ, Tang D, Tische C, and Alkema PK. Pattern formation of vascular smooth muscle cells subjected to nonuniform fluid shear stress: mediation by the gradient of cell density. *Am J Physiol Heart Circ Physiol* 285: H1072–H1080, 2003.
 25. Liu SQ, Tische C, Dalin T, and Alkema P. Pattern formation of vascular smooth muscle cells subject to nonuniform fluid shear stress: role of platelet-derived growth factor β -receptor and Src. *Am J Physiol Heart Circ Physiol* 285: H1081–H1090, 2003.
 26. Liu SQ, Zhong L, and Goldman J. Control of the shape of a thrombus-neointima-like structure by blood shear stress. *J Biomech Eng* 124: 30–36, 2002.
 27. Long Q, Xu XY, Collins MW, Bourne M, and Griffith TM. Magnetic resonance image processing and structured grid generation of a human abdominal bifurcation. *Comput Methods Programs Biomed* 56: 249–259, 1998.
 28. McLean DR and Eigler NL. Stent design: implications for restenosis. *Rev Cardiovasc Med* 3, Suppl 5: S16–S22, 2002.
 29. Moore JA, Rutt BK, Karlik SJ, Yin K, and Ethier CR. Computational blood flow modeling based on in vivo measurements. *Ann Biomed Eng* 27: 627–640, 1999.
 30. Moore, JE Jr, Xu C, Glagov S, Zarins CK, and Ku DN. Fluid wall shear stress measurements in a model of the human abdominal aorta: oscillatory behavior and relationship to atherosclerosis. *Atherosclerosis* 110: 225–240, 1994.
 31. Morice MC, Serruys PW, Sousa JE, Fajadet J, Ban Hayashi E, Perin M, Colombo A, Schuler G, Barragan P, Guagliumi G, Molnar F, and Falotico R; RAVEL Study Group. Randomized Study with the Sirolimus-Coated Bx Velocity Balloon-Expandable Stent in the Treatment of Patients with de Novo Native Coronary Artery Lesions. A randomized comparison of a sirolimus-eluting stent with a standard stent for coronary revascularization. *N Engl J Med* 346: 1773–1780, 2002.
 32. Murata T, Hiro T, Fujii T, Yasumoto K, Murashige A, Kohno M, Yamada J, Miura T, and Matsuzaki M. Impact of the cross-sectional geometry of the post-deployment coronary stent on in-stent neointimal hyperplasia: an intravascular ultrasound study. *Circulation* 66: 489–493, 2002.
 33. Myers JG, Moore JA, Ojha M, Johnston KW, and Ethier CR. Factors influencing blood flow patterns in the human right coronary artery. *Ann Biomed Eng* 29: 109–120, 2001.
 34. Narayanaswamy M, Wright KC, and Kandarpa K. Animal models for atherosclerosis, restenosis, and endovascular graft research. *J Vasc Interv Radiol* 11: 5–17, 2000.
 35. Newman VS, Berry JL, Routh WD, Ferrario CM, and Dean RH. Effects of vascular stent surface area and hemodynamics on intimal thickening. *J Vasc Interv Radiol* 7: 387–393, 1996.
 36. Nichols WW and O'Rourke MF. *McDonald's Blood Flow in Arteries: Theoretical Experimental and Clinical Principles*. New York: Oxford University Press, 1998.
 37. Orford JL, Selwyn AP, Ganz P, Popma JJ, and Rogers C. The comparative pathobiology of atherosclerosis and restenosis. *Am J Cardiol* 86: 6H–11H, 2000.
 38. Prakash S and Ethier CR. Requirements for mesh resolution in 3D computational hemodynamics. *J Biomech Eng* 123: 134–144, 2001.
 39. Qiu Y and Tarbell JM. Numerical simulation of oxygen mass transfer in a compliance curved tube model of a coronary artery. *Ann Biomed Eng* 28: 26–38, 2000.
 40. Rajagopal V and Rockson SG. Coronary restenosis: a review of mechanisms and management. *Am J Med* 115: 547–553, 2003.
 41. Rivers ML, Sutton S, and Eng P. Geoscience applications of x-ray computed microtomography. *Proc SPIE Develop X-ray Tomogr II* 3772: 78–86, 1999.
 42. Robb RA, Hanson DP, Karwoski RA, Larson AG, Workman EL, and Stacy MC. Analyze: a comprehensive, operator-interactive software package for multidimensional medical image display and analysis. *Comput Med Imaging Graph* 13: 433–454, 1989.
 43. Rogers C and Edelman ER. Endovascular stent design dictates experimental restenosis and thrombosis. *Circulation* 91: 2995–3001, 1995.
 44. Rogers C, Edelman ER, and Simon DI. A mAb to the beta2-leukocyte integrin Mac-1 (CD11b/CD18) reduces intimal thickening after angioplasty or stent implantation in rabbits. *Proc Natl Acad Sci USA* 95: 10134–10139, 1998.
 45. Shammash NW, Kapalis MJ, Dippel EJ, Jerin MJ, Lemke JH, Patel P, and Harris M. Clinical and angiographic predictors of restenosis following renal artery stenting. *J Invasive Cardiol* 16: 10–13, 2004.
 46. Van Belle E, Tio FO, Couffinhal T, Maillard L, Pesseri J, and Isner JM. Stent endothelialization: time course, impact of local catheter delivery, feasibility of recombinant protein administration, and response to cytokine expedition. *Circulation* 95: 438–448, 1997.
 47. Vernhet H, Juan JM, Demaria R, Olivia-Lauraire M, Senac J, and Dautat M. Acute changes in aortic wall mechanical properties after stent placement in rabbits. *J Vasc Interv Radiol* 11: 634–638, 2000.
 48. Virmani R, Kolodgie FD, Farb A, and Lafont A. Drug eluting stents: are human and animal studies comparable? *Heart* 89: 133–138, 2003.
 49. Welt FG and Rogers C. Inflammation and restenosis in the stent era. *Arterioscler Thromb* 22: 1769–1776, 2002.
 50. Wentzel JJ, Whelan DM, van der Giessen WJ, van Beusekom HM, Andhyiswara I, Serruys PW, Slager CJ, and Krams R. Coronary stent implantation changes 3-D vessel geometry and 3-D shear stress distribution. *J Biomech* 33: 1287–1295, 2000.